Korean J. Chem. Eng., 38(3), 617-623 (2021)
DOI: 10.1007/s11814-020-0700-5

pISSN: 0256-1115
eISSN: 1975-7220

Photocatalytic degradation characteristics of heterojunction SnO_2-Cu_xO nanopowders of methylene blue under UV light

Kiryung Eom*, Il Han Yoo*, Shankara Sharanappa Kalanur,†, and Hyungtak Seo*,**,†**

*Department of Energy Systems Research, Ajou University, Suwon 16499, Korea
**Department of Materials Science and Engineering, Ajou University, Suwon 16499, Korea
(*Received 6 June 2020 • Revised 19 October 2020 • Accepted 28 October 2020*)

Abstract−p-n heterojunction was constructed using p-type Cupric oxide (CuO) and n-type Tin (IV) oxide (SnO_2) nanoparticles using chemical synthesis and annealing method. The synthesized SnO_2-CuO nanoparticles were characterized using X-ray diffraction (XRD), transmission electron microscopy (TEM), scanning electron microscopy (SEM), X-ray photoelectron spectroscopy (XPS), etc. The methylene blue (MB) degradation ability of the synthesized SnO_2-CuO nanocomposite was investigated under UV illumination. Compared to the undoped SnO_2, the SnO_2-CuO p-n heterojunction exhibited enhanced MB degradation capability due the effective separation of electron-holes pair that suppresses the recombination. Based on the experimental results, the charge dynamics and the probable dye degradation mechanism via SnO_2-CuO nanoparticles was proposed.

Keywords: SnO_2, CuO, Photocatalyst, Heterojunction, Nanoparticles

INTRODUCTION

The chemical, agricultural, transportation, textile and many other industries play a crucial role in the development of modern civilization. However, in various sectors this could also lead to various kinds of environmental pollution, posing a serious threat for the future. Specifically, the contamination caused in running water via the various pollution routes poses a serious threat to living beings [1,2]. Therefore, tremendous research is essential and actively underway to establish sustainable, clean and efficient technologies to degrade or clean the water sources. Among the various methodologies utilized for pollutant degradation processes, the photocatalytic method using a photocatalyst is known to be sustainable, clean and environmentally friendly [3-5]. Here, the photocatalyst refers to the semiconductor material that decomposes toxic organic substances using photogenerated electrons and holes as a reducing/oxidizing agent under the irradiation of light [6].

Among the numerous materials reported so far, titanium oxide (TiO_2) has been studied widely and actively due to its biological and chemical inertness, strong oxidizing power, non-toxicity and long-term stability against corrosion [7-9]. However, TiO_2 as a photoactive and catalyst material faces some limitations, such as fast recombination of the photo-generated electron-hole pairs, insufficient absorption of incident sunlight due to the wide bandgap of 3.2 eV [10]. To overcome the limitation of TiO_2, various strategies have been proposed so as to increase the charge separation by preventing recombination and to reduce the bandgap to increase the light absorption ability which directly affects the efficiency of the photocatalyst. For example, doping method is routinely used to overcome the limitations of oxide semiconductor photocatalysts such as zinc oxide (ZnO), SnO_2, CuO, cuprous oxide (Cu_2O) and TiO_2 [10-13]. In addition, compositing semiconductor materials to form heterostructures could also be implemented to overcome the limitation of commonly used metal oxide materials. Furthermore, several other strategies could also be implemented to improve photocatalytic activity, such a, reducing particle size and engineering specific nanostructures [14-17].

SnO_2 is an n-type material having a large bandgap of about 3.8 eV that is used actively in photocatalytic applications [18]. Due to the wide band gap, the photocatalytic activity of SnO_2 is found to be in UV region of incident light. Moreover, the photocatalytic activity of SnO_2 is limited due to the poor separation of photogenerated charges. In this work, SnO_2 is combined with CuO material to increase its photocatalytic MB dye degradation activity via forming a heterojunction system. Importantly, by combining n-type SnO_2 with p type CuO, p-n heterojunction will be obtained that facilitates the effective separation of electron-hole pair and thus improves the efficiency photocatalytic activity.

MATERIALS AND METHODS

1. Synthesis of Pure SnO_2 and SnO_2-CuO Nanoparticles

SnO_2 nanoparticles were synthesized using a hydrothermal method. Briefly, 0.9 g $SnCl_4$-$5H_2O$ and 0.8 g NaOH were dissolved in 20 ml ethanol and then 0.16 g citric acid was added to the solution and stirred vigorously for 30 minutes using a magnetic stirrer. The mixture was transferred to Teflon well of the autoclave filling 70% of its volume and heated at 190 °C for 24 hours. After the completion of the synthesis the autoclave was cooled naturally to room temperature. A 10 °C per minute temperature ramp was used to reach 190 °C. The final powder was filtered, washed repeatedly with ethanol and cleaned, and finally dried at 60 °C to obtain

†To whom correspondence should be addressed.
E-mail: shankarask@ajou.ac.kr, hseo@ajou.ac.kr

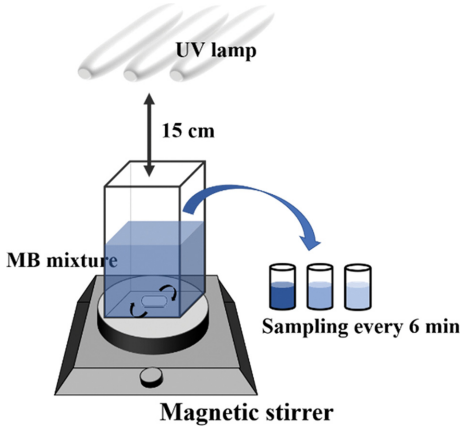

Fig. 1. Schematic diagram of UV reaction applied to photocatalyst degradation.

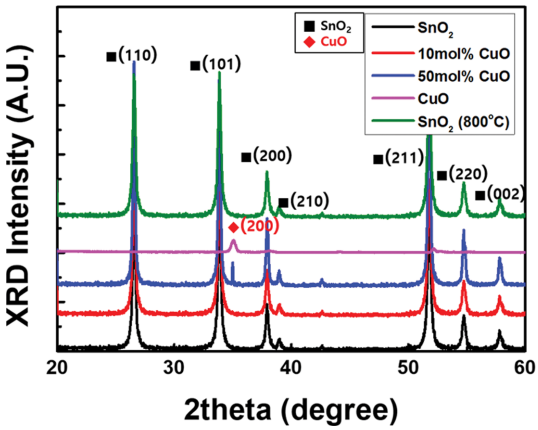

Fig. 2. XRD patterns of pure SnO_2 (black), CuO (pink) and 6 wt% CuO combined SnO_2 (red) CuO, (blue) 35 wt% CuO combined SnO_2 and after annealed SnO_2 (green).

SnO_2 nanopowder [19].

The SnO_2-CuO heterojunction nanoparticles were obtained through a chemical synthesis and annealing method. Briefly, 2 mmol of SnO_2 nanoparticles and $Cu(NO_3)_2$-$3H_2O$ were mixed with 0.2 and 1 mmol (6 wt%, 35 wt% CuO), respectively, in 50 ml of ethanol. The mixture dispersed evenly using ultrasonic waves for 1 h and then was further stirred for 2. The produced green precipitate was separated by centrifugation for 20 minutes at 6,000 rpm. The separated product was dried at 60 °C for at least 3 hours, and then annealed at 800 °C/2 h with 10 °C per minute ramp to yield black SnO_2-CuO product. Samples of pure CuO were prepared under the same conditions without the addition of SnO_2 nanoparticles.

2. Characterization

The crystal structure was obtained by X-ray diffraction (XRD/Rikagu, with a 2θ scan from 20° to 80°, Cu-Kα (λ=1.5414 Å)). Field emission scanning electron microscopy (FESEM/Hitachi S-4800 (Japan)) and transmission electron microscopy (TEM) were used to determine the micromorphism, and EDX (JEOL JEM-2100F (USA)) was further measured to determine the effect of CuO. The absorbance changes during the dye degradation experiments were measured using UV-vis spectroscopy (Cary 5000, Agilent, USA). The theta probe base system, Thermo Fisher Scientific Co., USA, was used to measure X-ray photoelectron spectroscopy (XPS).

A schematic diagram of a simple experimental method is shown in Fig. 1. Note that the photocatalytic dye degradation experiments were performed using various amounts of CuO doped SnO_2 samples and detailed characterization was only performed on those samples which showed higher degradation efficiency. Briefly, 0.1 g (20 ppm) of MB was taken in 50 ml DI water and mixed with 0.5 mg of SnO_2-CuO nanoparticles. After stirring for about 30 minutes, MB solution containing photocatalyst was taken in 100 ml pyrex glass bottle and illuminated with UV (18 W Hg lamp with main emission wavelength of about 365 nm) light irradiation. The temperature of the sample was fixed at room temperature of about 23 °C, and the sample was kept constant with a stirrer. The samples were collected every 6 minute interval in chronological order and then analyzed using UV-vis spectroscopy in the wavelength range of 300 to 1,000 nm.

RESULTS AND DISCUSSION

The XRD pattern of undoped SnO_2 and CuO doped SnO_2 is shown in Fig. 2, where the XRD results of pure SnO_2 synthesized, $Cu(NO_3)_2$-$3H_2O$ with 0.2 mmol (6 wt% CuO) and 1 mmol (35 wt% CuO). The XRD peaks exhibited by the undoped SnO_2 were ascribed to the pure rutile structure of SnO_2 (JCPDS Card No. 41-1445). For the 6 wt% of CuO doped SnO_2 samples, no characteristic peaks related to CuO were observed and the XRD pattern appeared to be similar to the pure SnO_2. This indicates that the Cu is incorporated into SnO_2 lattice structure. However, the 35 wt% CuO doped

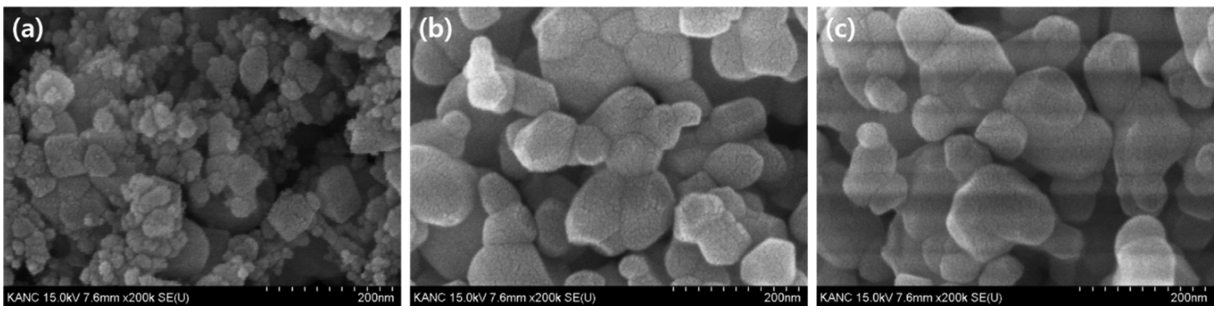

Fig. 3. SEM image of (a) pure SnO_2, (b) 6 wt% CuO and (c) 35 wt% CuO combined SnO_2.

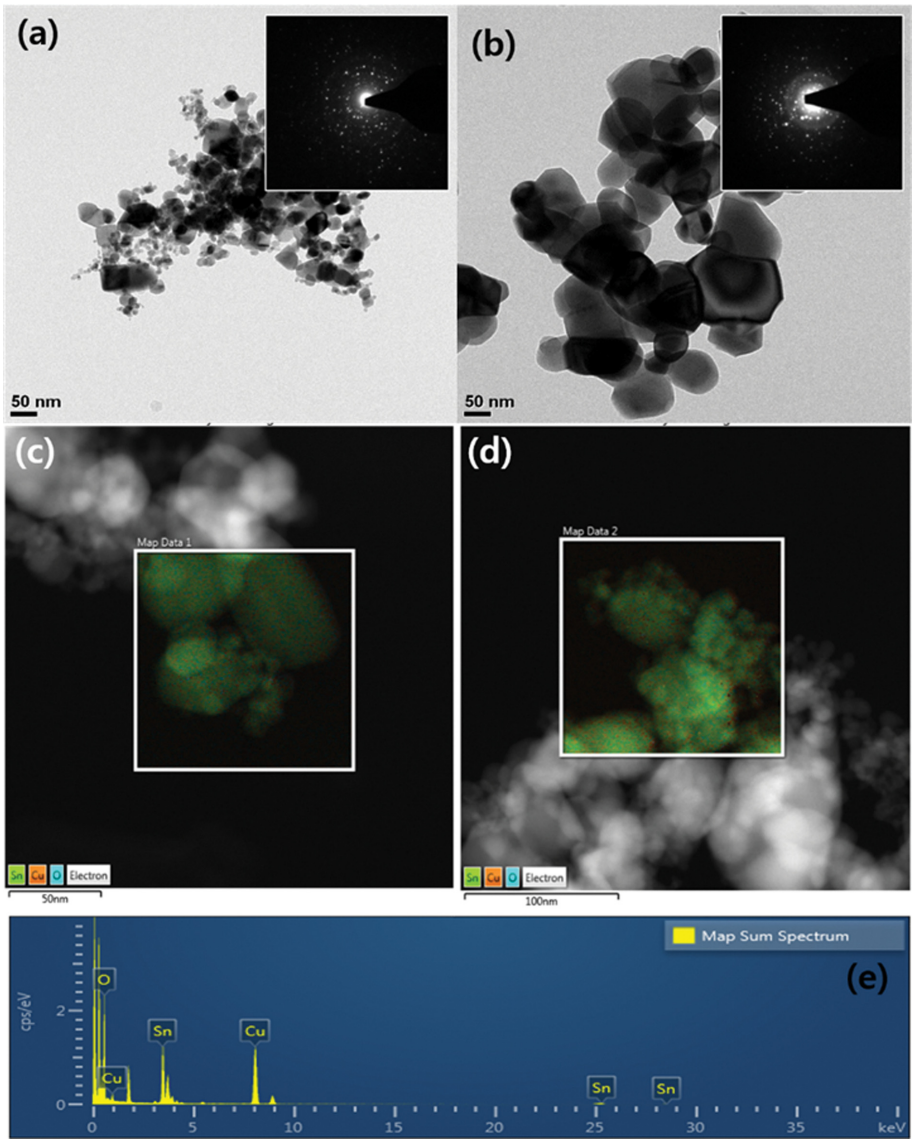

Fig. 4. TEM image of (a) pure SnO_2, (b) 6 wt% CuO combined SnO_2, (c) EDX data of 6 wt% CuO combined SnO_2 and (d), (e) 35 wt% CuO combined SnO_2.

SnO_2 samples show a small but noticeable peak of CuO at about 35° theta degree. The XRD pattern clearly indicates the CuO peak corresponding to (002) plane of the monoclinic CuO (JCPDS Card No. 45-0937) along with SnO_2 peaks, which confirms the composite formation.

SEM measurements were performed to understand the change in morphology of SnO_2 before and after the CuO doping (Fig. 3). Pure SnO_2 exhibited particle morphology of different shapes with varying diameter between 5 to 100 nm (Fig. 3(a)). Interestingly, the 35 wt% CuO doped SnO_2 exhibited relatively bigger particle size between 100-200 nm. Statistical particle size was calculated using the Scherrer equation [20]. First, in the case of pure SnO_2, the average particle size was measured to be 76.2 nm, and in the case of SnO_2 through heat treatment, the average size was increased to about 142 nm. The increase in the particle size after CuO-doping could be ascribed to the higher heat treatment process that could lead to particle agglomeration [21]. The increase in crystal size of SnO_2 was further evident from the previously shown XRD peaks, which show high intensity compared to undoped SnO_2 particles. Furthermore, the particles were found to be arranged to form the porous structure, which allows higher surface area for the interaction with contaminants, which could influence its degradation activity.

Fig. 4 shows the high resolution TEM image of SnO_2-CuO composite, confirming its particle size and morphology. In accordance with the previously shown SEM images, the incorporation of CuO in SnO_2 causes an increase in the particle size as seen in the Fig. 4(b). Furthermore, energy dispersive X-ray (EDX) mapping analysis was used to understand the distribution of each element in the SnO_2-CuO composite. The mapping images indicate that the CuO was embedded uniformly on to the SnO_2 nanoparticles and the quantitative analysis revealed the 6 wt% CuO in SnO_2. The inset in Fig. 4(a), (b) shows the selected area electron diffraction (SAED)

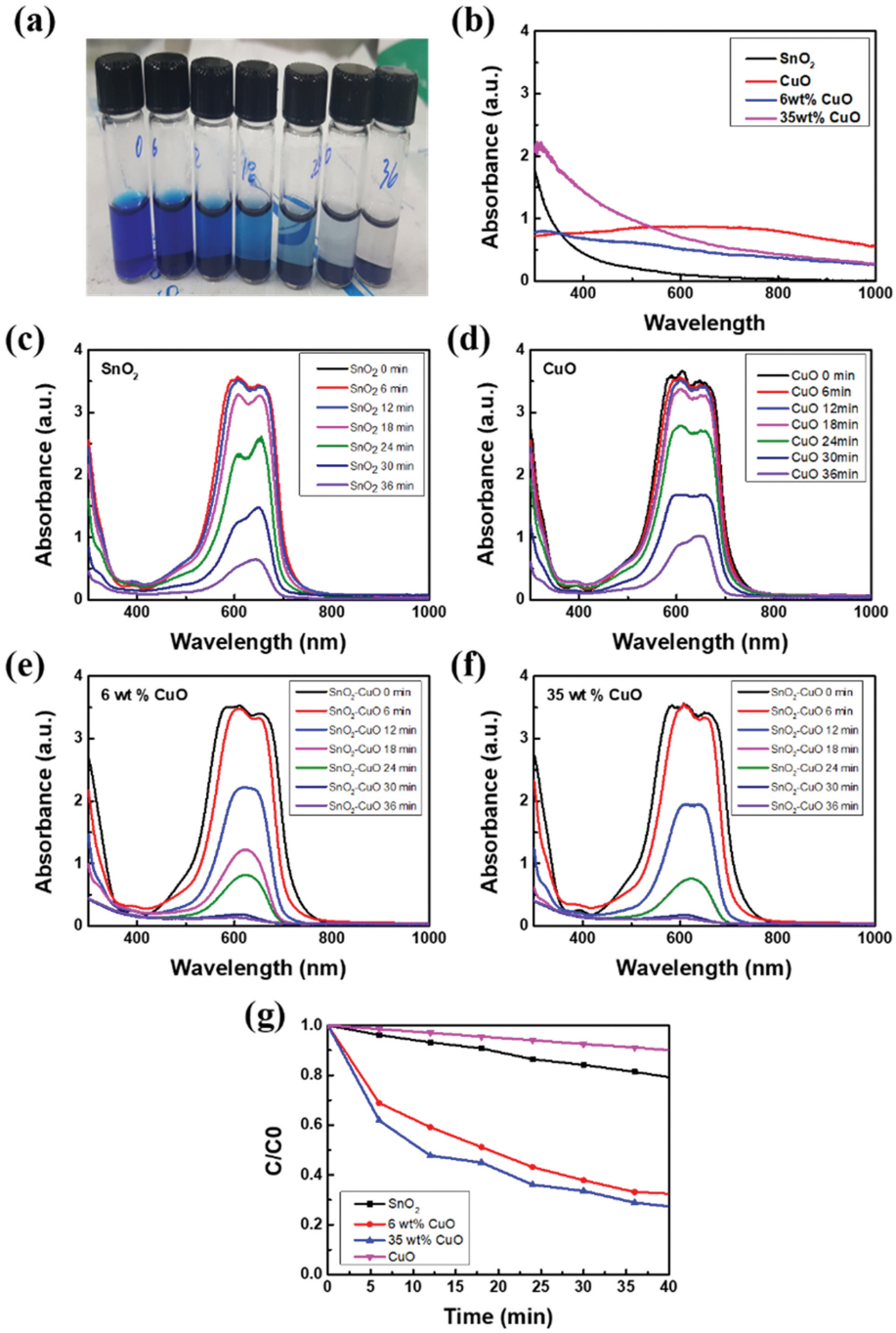

Fig. 5. (a) Photographic image of methylene blue degradation over time for 35 wt% CuO doped SnO_2 (b) absorbance data for each samples and MB in presence of (c) pure SnO_2, (d) pure CuO, (e) 6 wt% CuO doped SnO_2 (f) 35 wt% CuO doped SnO_2 measured at different time intervals, (g) Plot of C/C0 vs time for SnO_2-CuO.

image, indicating the crystallinity of the samples. In addition, the sample annealed at 800 °C for 2 hours shows high crystallinity as evident from SAED patterns.

Photocatalytic MB degradation studies were performed to evaluate the effect of CuO combined SnO_2 as shown in Fig. 5. Note that the photocatalytic dye degradation experiments were performed using various amounts of CuO doped SnO_2 samples, and a detailed characterization was only performed on those samples that show higher degradation efficiency. The absorbance measurements of the dye solution containing SnO_2-CuO nano powder were collected every 6 minutes. Fig. 5 shows the absorbance results of each sample. In the case of pure SnO_2, the peak of absorption increases near 400 nm. On the other hand, pure CuO shows a relatively high absorbance between 400 and 800 nm, but shows an absorption intensity of a certain level or more in the entire wavelength range. In the sample combined with CuO, after heat treatment at a high tempera-

ture of 800 °C the overall absorbance increases as the SnO_2 particles turn black, and likewise the absorption peak increases near 400 nm. From Fig. 5(g), 35 wt% CuO doped SnO_2 exhibits significantly higher photocatalytic activity compared to pure SnO_2. Furthermore, the 6 wt% CuO doped SnO_2 also exhibits almost similar dye degradation activity compared to 35 wt% CuO doped SnO_2. Fig. 5(c) and (e) show the absorbance plot of SnO_2 and 35 wt% of CuO doped SnO_2 indicating dye degradation capability. That is, compared to pure SnO_2, the CuO doped SnO_2 shows increased rate of dye degradation, indicating significant decrease in the absorbance values. Note that the absorbance curve of the dye remains the same before the degradation. However, the absorbance curve shape changes with the gradual dye degradation with time. This indicates that state of aggregation and surface interaction between the dye and the degradant is different on SnO_2 and CuO doped SnO_2. Importantly, the CuO doped SnO_2 provides more feasible surface property for significantly high dye degradation capability. The dye degradation experiments were carried out in same optimized conditions both in the presence of SnO_2 and CuO doped SnO_2. Hence the change in shape of absorbance curves solely depends on the degradation capability of the SnO_2 and CuO doped SnO_2. On the other hand, the 35 wt% of CuO in SnO_2 forms p-n junction heterojunction containing p-type CuO and n-type SnO_2. In addition, the photocatalytic property of pure CuO shows lower results than that of pure SnO_2 nanoparticles. As a result, SnO_2 combined with CuO forms a p-n heterojunction, and the synergistic effect increases the properties of the photocatalyst. Such a localized p-n junction was found to increase the effective separation of electron-hole pairs and that inhibits the recombination, leading to higher photocatalytic efficiency [22]. Based on the above results, the optimum photocatalytic activity was observed at 35 wt% CuO embedded in SnO_2.

XPS measurements were performed to analyze the chemical state CuO doped SnO_2 samples (Fig. 6). The binding energy of all spectra was corrected with respect to C1s peak at 248.8 eV. Fig. 6(a) and (b) show the deconvoluted XPS high resolution spectra of Cu2p peaks for 6 wt% and 35 wt% CuO doped SnO_2, respectively. The binding energy value of $Cu2p_{3/2}$ at 933 eV was found to be in agreement with the literature reports [23]. Two satellite peaks associated with $Cu2p_{3/2}$ at binding energy values of ~942 eV were also observed. Both the samples (6 and 35 wt% CuO) showed Cu^{1+} peak arising from Cu_2O and Cu^{2+} peak related to CuO moiety, indicating the presence of mixed phase of Cu_xO. Furthermore, the intensity of the satellite peak at ~942 eV indicates the dominant presence of CuO phase [23]. Integrating peak areas in 35 wt% CuO (Fig. 6(b)) sample showed the presence of 61±2% Cu^{2+} and

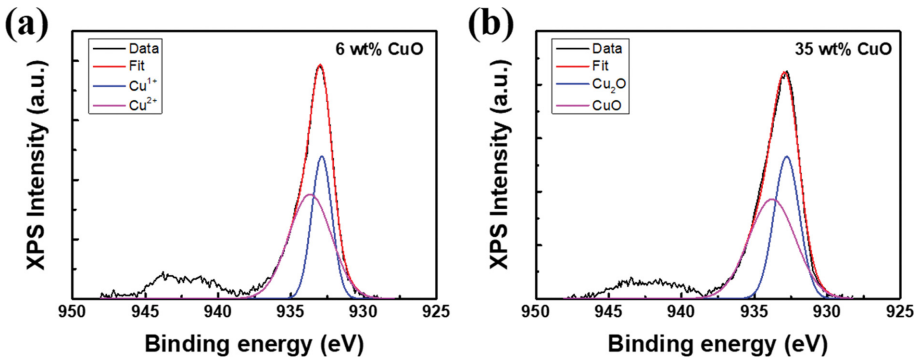

Fig. 6. Deconvoluted XPS high resolution spectra of Cu2p peaks obtained from (a) 6 wt% CuO, (b) 35 wt% CuO doped SnO_2.

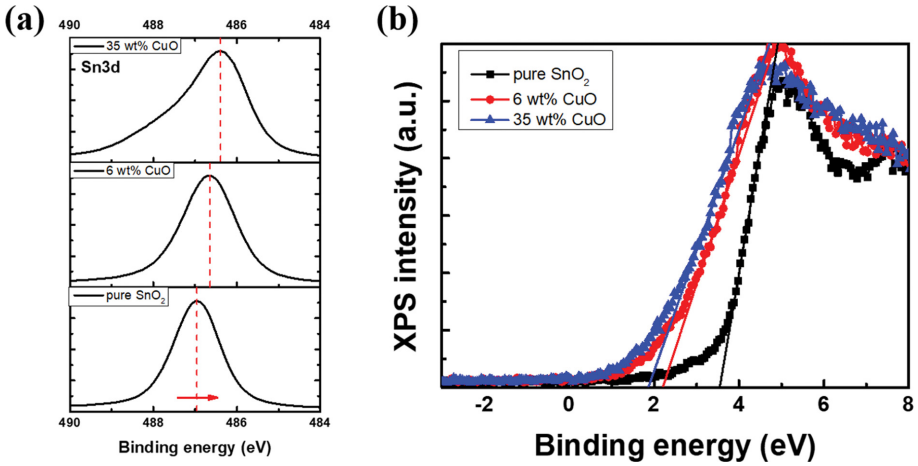

Fig. 7. (a) High resolution XPS peak of Sn3d for undoped and CuO doped SnO_2. (b) XPS valence band plot of spectra of undoped and CuO doped SnO_2.

39±2% Cu^{1+}, respectively. Whereas, in the 6 wt% CuO (Fig. 6(a)) sample, Cu^{2+} was noted to be 56±2% and Cu^{1+} was 44±2%. This indicates that the 35 wt% CuO sample contains 5% more characteristics of CuO properties. Note that the percentage of the presence of Cu^{2+} and Cu^{1+} was taken as the average of several (at least 4) measurements.

Similarly, high resolution XPS was used to study the Sn3d peak of undoped and CuO doped SnO_2 as shown Fig. 7(a). The undoped SnO_2 exhibited the characteristic $Sn3d_{5/2}$ peak at a binding energy value of 487 eV. Upon CuO doping the $Sn3d_{5/2}$ peak was found to be shifted towards lower binding energy. This was in accordance with the previous studies, indicating that the agglomeration of SnO_2 with dopant tends to shift the binding energy values towards lower values. This also indicates the presence of the CuO on the surface layer of SnO_2 [24,25]. Furthermore, XPS valence band edge (VBE) analysis was performed for the undoped and SnO_2 doped samples, as shown in Fig. 7(b). The undoped SnO_2 showed VBE value at about 3.5 eV, indicating strong n-type characteristic as the band gap value of pure SnO_2 is reported to be 3.7 eV [18]. After the doping of 6 and 35 wt% of CuO, the VBE value was found to be shifted to 2.2 eV and 1.9 eV, respectively. This indicates the successful incorporation of CuO, which is p-type material.

Based on the above results, the photocatalytic MB dye degradation mechanism of SnO_2-CuO composite under UV light illumination is shown in Fig. 8. During the illumination on CuO embedded SnO_2, the photogenerated electron hole pair is formed both in SnO_2 and CuO materials separately. Due the band alignments and the formed p-n junction heterojunction, the photogenerated electrons (e^-) at the CB band of CuO will be transferred to CB of SnO_2 and at the same time the photogenerated holes (h^+) from VB of SnO_2 are moved towards the VB of CuO. Here the presence of p-n junction interface between the SnO_2 CuO allows the efficient separation of electron-hole pairs, and thus provides a driving force to selectively transfer electrons-holes to the surface of the photocatalyst. Ultimately, these photogenerated electron hole pairs will be efficiently involved in dye degradation activity (Fig. 8). Specifically, the photo-generated electrons migrate to the surface and react with oxygen or dissolved oxygen in the solution to produce active $\bullet O^{2-}$ radicals. Simultaneously, holes migrating towards the surface act as oxidants and react with water to produce •OH radicals. Thus, both the $\bullet O^{2-}$ and •OH radicals act as powerful reducing and oxidizing agents for dye, respectively. Here, the active oxygen radicals attack the benzene ring of MB dye and reconstitute it into decomposition compounds (peroxy derivatives, hydroxylated derivatives).

CONCLUSION

CuO embedded SnO_2-CuO nanoparticles were prepared by hydrothermal method. The synthesized materials were characterized using XRD, SEM, TEM and XPS measurement. The morphological results indicate that the particle size of SnO_2 increased after the addition of CuO. Through XPS analysis, the states present in Cu_xO were investigated and found that the composite photocatalyst contains a mixture of Cu_2O and CuO phase. The photocatalytic dye degradation efficiency of the SnO_2-CuO composites was evaluated by decomposition of MB under UV illumination. Compared to pure SnO_2, the SnO_2-CuO composite exhibited enhanced dye degradation activity due to the formation of p-n heterojunctions, which facilitates effective charge separation of electron-hole pairs, thus reducing recombination. Based on the results, the probable charge transfer mechanism for dye degradation was explained.

ACKNOWLEDGEMENTS

This work was supported by the basic Research & Development program [NRF-2019R1A2C2003804 and NRF-2017R1D1 A1B03035201] of the Ministry of Science and ICT, Republic of Korea. This work was also supported by Ajou University.

REFERENCES

1. L. Gnanasekaran, R. Hemamalini, R. Saravanan, K. Ravichandran, F. Gracia, S. Agarwal and V. K. Gupta, *J. Photochem. Photobiol. B: Biol.*, **173**, 43 (2017).
2. X.-J. Zheng, Y.-J. Wei, L.-F. Wei, B. Xie and M.-B. Wei, *Int. J. Hydrogen Energy*, **35**, 11709 (2010).
3. N. F. Khairol, N. Sapawe and M. Danish, *Mater. Today: Proceedings*, **19**, 1333 (2019).

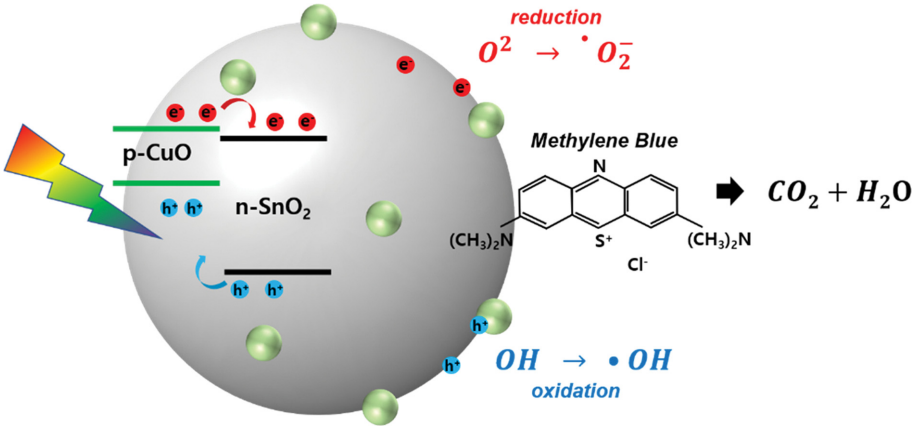

Fig. 8. Schematic diagram of MB decomposition using SnO_2-CuO composite.

4. P. D. Shivaramu, A. Patil, M. Murthy, S. Tubaki, M. Shastri, S. Manjunath, V. Gangaraju and D. Rangappa, *Mater. Today: Proceedings*, **4**, 12314 (2017).
5. H.-l. Xia, H.-S. Zhuang, T. Zhang and D.-C Xiao, *J. Environ. Sci.*, **19**, 1141 (2007).
6. A. Enesca, L. Isac and A. Duta, *Thin Solid Films*, **542**, 31 (2013).
7. Y. Bessekhouad, D. Robert and J. Weber, *J. Photochem. Photobiol. A: Chem.*, **163**, 569 (2004).
8. S. Kohtani, M. Tomohiro, K. Tokumura and R. Nakagaki, *Appl. Catal. B: Environ.*, **58**, 265 (2005).
9. A. H. Mamaghani, F. Haghighat and C.-S. Lee, *Appl. Catal. B: Environ.*, **203**, 247 (2017).
10. A. Zaleska, *Recent Patents on Eng.*, **2**, 157 (2008).
11. M. Ahmad, E. Ahmed, Y. Zhang, N. Khalid, J. Xu, M. Ullah and Z. Hong, *Curr. Appl. Phys.*, **13**, 697 (2013).
12. M. V. Dozzi and E. Selli, *J. Photochem. Photobiol. C: Photochem. Rev.*, **14**, 13 (2013).
13. N. L. Gavade, S. B. Babar, A. N. Kadam, A. D. Gophane and K. M. Garadkar, *Ind. Eng. Chem. Res.*, **56**, 14489 (2017).
14. R. Kumar, G. Kumar and A. Umar, *Mater. Lett.*, **97**, 100 (2013).
15. J. Lee, Y. Lee, J. K. Youn, H. B. Na, T. Yu, H. Kim, S. M. Lee, Y. M. Koo, J. H. Kwak and H. G. Park, *Small*, **4**, 143 (2008).
16. C. Lin, Y. Song, L. Cao and S. Chen, *J. Chin. Adv. Mater. Soc.*, **1**, 188 (2013).
17. R. Saravanan, S. Karthikeyan, V. Gupta, G. Sekaran, V. Narayanan and A. Stephen, *Mater. Sci. Eng.: C*, **33**, 91 (2013).
18. O. Mounkachi, E. Salmani, M. Lakhal, H. Ez-Zahraouy, M. Hamedoun, M. Benaissa, A. Kara, A. Ennaoui and A. Benyoussef, *Solar Energy Mater. Solar Cells*, **148**, 34 (2016).
19. B. Babu, A. Kadam, R. Ravikumar and C. Byon, *J. Alloys Compd.*, **703**, 330 (2017).
20. I. Leontyev, D. Y. Chernyshov, V. Guterman, E. Pakhomova and A. Guterman, *Appl. Catal. A: Gen.*, **357**, 1 (2009).
21. N. T. Thanh, N. Maclean and S. Mahiddine, *Chem. Rev.*, **114**, 7610 (2014).
22. M. T. Uddin, Y. Nicolas, C. Olivier, T. Toupance, L. Servant, M. M. Müller, H.-J. Kleebe, J. R. Ziegler and W. Jaegermann, *Inorg. Chem.*, **51**, 7764 (2012).
23. S. Poulston, P. Parlett, P. Stone and M. Bowker, *Surf. Interface Anal.*, **24**, 811 (1996).
24. W. Chen, Q. Li, H. Gan and W. Zeng, *Adv. Appl. Ceram.*, **113**, 139 (2014).
25. M. Chuai, X. Chen, K. Zhang, J. Zhang and M. Zhang, *J. Mater. Chem. A*, **7**, 1160 (2019).